Reactive and Functional Polymers 208 (2025) 106149

Contents lists available at ScienceDirect

Reactive and Functional Polymers

journal homepage: www.elsevier.com/locate/react

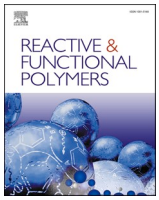

Advancements in radiation-induced grafted anion-exchange membranes: Controlling pre-irradiation parameters of high-density polyethylene for enhanced fuel cell performance and durability

Andrey S. Barbosa [a,*], Ana Laura G. Biancolli [a], Bianca P.S. Santos [a], Jean-Jacques Bonvent [b], Daniel Hermida-Merino [c,d], Elisabete I. Santiago [a,*]

[a] Nuclear and Energy Research Institute, IPEN/CNEN, 05508-000 São Paulo, Brazil
[b] Center for Natural and Human Sciences, Federal University of ABC, 09210-580 Santo André, Brazil
[c] Netherlands Organisation for Scientific Research (NWO), c/o ESRF BP 220, DUBBLE CRG/ESRF, CEDEX, 38043 Grenoble, France
[d] Departamento de Física Aplicada, CINBIO, Universidade de Vigo, Campus Lagoas-Marcosende, 36310 Vigo, Spain

ARTICLE INFO

Keywords:
Anion-exchange membrane
AEMFC
HDPE
SAXS
Radiation-induced grafting

ABSTRACT

Manufacturing anion-exchange membranes (AEMs) with high durability is a current challenge for low-temperature alkaline fuel cells. In this work, a series of AEMs based on high-density polyethylene (HDPE) is synthetized by radiation-induced grafting (RIG) method considering various pre-irradiation conditions, such as temperature and atmosphere. The AEMs are extensively characterized, including assessments of the degree of grafting (DoG), ion-exchange capacity (IEC), water absorption properties, and hydroxide conductivity. Additionally, their molecular structure and thermal and mechanical properties are evaluated. Techniques, such as atomic force microscopy (AFM) and synchrotron small angle x-ray scattering (SAXS), are employed for analysis of AEMs morphology. Finally, the AEMs are applied in an H_2-O_2 anion-exchange membrane fuel cell (AEMFC) and subjected to a short-term stability test. Among the tested AEMs, the one pre-irradiated at low temperature (−10 °C) and air atmosphere exhibits excellent AEMFC performance of 2.1 W cm^{-2}. This sample possesses high OH^- conductivity of 208 mS cm^{-1} at 80 °C, and the stability test shows a conductivity loss of −0.06 % h^{-1} during 100 h under reduced relative humidity (80 %). Applying an accurate protocol for controlling pre-irradiation parameters can effectively reduce the irradiation degradation effects.

1. Introduction

Hydrogen has been considered an important candidate for clean energy technologies in recent years [1]. Among them, fuel cells are a great example of net-zero emission technology that uses hydrogen as an energy source with high efficiency [2]. Over the last years, anion-exchange membrane fuel cells (AEMFCs) have received real emphasis, mainly when compared to the extensively researched proton-exchange membrane fuel cells (PEMFCs), due to their fast kinetics oxygen reduction reaction (ORR) and its potential for building platinum-free devices [3,4]. These factors are crucial to lowering the expenses of fuel cell technology, opening up the possibilities of achieving end-application, such as fuel cell electric vehicles and stationary fuel cell power systems competitively. However, anion-exchange membranes (AEMs), which are the polymeric electrolytes of such devices, are frequently associated with low chemical and mechanical stabilities in alkaline medium of AEMFCs. Currently, this factor has been suggested as the most pivotal challenge to consolidate this technology.

The AEM stability is affected by continuous degradation caused by both alkaline medium and temperature during fuel cell operation due to the OH^- attack in the polymer backbone and/or quaternary ammonium group (QA) [5]. The QA degradation diminishes the ion-exchange capacity (IEC) of AEM compromising the AEMFC performance [5]. In this context, continuous efforts have been made to produce more stable AEMs, such as the use of different QAs (trimethylamine, methylpiperidine, imidazolium, morpholinium, guanidinium) as well as increasing the steric hindrance to avoid OH^- attack in the bulky groups or increasing the QA side chain [6–10]. The formation of crosslinking between polymer chains or QAs is also an attempt to reinforce the structure and improve the mechanical properties of AEMs, resulting in higher

* Corresponding authors.
E-mail addresses: andreybarbosa@alumni.usp.br (A.S. Barbosa), elisabete.santiago@usp.br (E.I. Santiago).

https://doi.org/10.1016/j.reactfunctpolym.2025.106149
Received 5 October 2024; Received in revised form 18 December 2024; Accepted 1 January 2025
Available online 9 January 2025

stability and durability [11–13]. On the other hand, excessive crosslinking diminishes the ion conductivity causing a decrease in AEMFCs performance [14]. Therefore, a balance between conductivity and enhanced physicochemical and mechanical properties is crucial for the consolidation of AEMFC technology.

Different AEM synthesis strategies as polycondensation, Friedel-Crafts, Click reaction, and others have been reported [15–19]. One of the approaches is to use the radiation-induced grafting (RIG) technique [7,20–23]. RIG is a simple methodology to prepare AEMs using pre-fabricated films, in which radiation sources, such as electron beam, ultraviolet or gamma rays, act in providing radical species for the copolymerization process. In general, RIG is separated into two methods: i) simultaneous method (SM), in which the pre-fabricated film and monomer solutions are irradiated together to promote the grafting at the same time; and ii) pre-irradiation method (PIM), in which the pre-fabricated film is first irradiated and sequentially exposed to the grafting process in another step [24–26]. PIM has been preferably used due to the higher availability of e-beam irradiators compared to gamma beams, also due to the possibility of controlling grafting reaction parameters (temperature and time, for example), and lower formation of homopolymer when compared to SM [26]. Furthermore, our recent work has shown that AEMs prepared by PIM present enhanced water management due to membranes' morphology, better mechanical properties, and promote higher AEMFC performances when compared to similar AEMs prepared by SM [26].

Several pre-fabricated polymeric films have been proposed for RIG-AEM preparation, such as fluorinated, partially-fluorinated, and non-fluorinated polymers [27–31]. Polyethylene (PE), a low-cost polyolefin commodity widely used in many industrial processes, is a promising material to synthesize AEM due to its good thermal, mechanical, and chemical stability. Additionally, PE material is easier to recycle than fluorinated polymers [6,32]. High density polyethylene (HDPE)-based RIG-AEMs have shown optimistic long-term durability in AEMFCs. Wang et al. [23] reported a degradation rate of 68 μV h^{-1} for an HDPE-based AEM under operation at 600 mA cm^{-2} for 440 h. In another work, Peng et al. [33] has shown longer durability for HDPE-based AEMFC with a degradation rate of 32 μV h^{-1} in 1000 h. Such results indicate that HDPE is a promising material to use as base polymer for AEM synthesis, since it possesses high alkaline resistance as well as superior thermal and mechanical properties [24,34,35].

The first preparation step of AEMs *via* PIM is the irradiation of films. However, until our previous study [36], there was a lack in the literature concerning the control of pre-irradiation of base polymer films used to manufacture AEMs. We have shown for low-density polyethylene (LDPE)-based AEMs that parameters, such as temperature, atmosphere, and dose, have a strong influence on AEMs' properties [36]. Indeed, the interaction of radiation with the polymer leads to the formation of radicals for grafting reaction, whereas other reactions involving radical species (mainly crosslinking and chain scission), which are strongly associated with AEMs' physicochemical and morphological properties, also can occur [37–39]. The extension of each reaction is given by nature and concentration of radicals generated, which in turn are dependent on the irradiation parameters. In addition, these parameters will dictate the availability of radicals for other processes or whether they will decay to neutrality.

The present study investigates how pre-irradiation parameters impact the AEMFC performance and stability of polyethylene-based AEMs prepared by RIG. Our last report showed that the pre-irradiation stage affects the physicochemical properties, fuel cell performance, and alkaline stability of low-density polyethylene-based AEMs [36]. The current report provides new insights into changing the nature of the polymer, as well as draws a correlation between the effects of pre-irradiation parameters in the nanostructure/morphology of pre-irradiated HDPE-based AEMs and fuel cell performance and AEM stability.

2. Materials and methods

2.1. Pre-irradiation of HDPE films

Commercial HDPE films (130 mm × 80 mm × 0.01 mm, Goodfellow) were pre-irradiated with radiation absorbed dose of 100 kGy with an electron beam accelerator DC1500/25/4 model JOB 188 from RDI-Radiation Dynamics Inc. USA. To obtain the absorbed dose necessary the beam current was adjusted to 5.74 mA with energy of 0.55 MeV. The samples were placed on the surface of a tray with a displacement speed of 6 m min^{-1}, this provided a dose rate of 39.97 kGy s^{-1}. In the present study, the pre-irradiation process was evaluated in N_2 and air atmospheres, and two temperature conditions - room temperature (RT, 25 °C) and low temperature (LT, ~ −10 °C). For irradiation in air and RT, the films were directly exposed to the e-beam, while the pre-irradiation in N_2 (99.992 %) was conducted by placing HDPE films inside a hermetic balloon with a unidirectional valve filled with N_2 before radiation exposure. A series of three cycles of filling and emptying were carried out to guarantee total air absence, and the balloon was checked for leaks. For the irradiation performed at low temperature (LT), the film was placed over a layer of dry ice. The surface temperature of the film, measured using an infrared laser thermometer, was −10 °C. Immediately after the irradiation process, the pre-irradiated samples were stored in an ultra-freezer at −45 °C for 24 h prior to grafting step to avoid the decay of radicals.

2.2. AEM preparation

The AEM preparation by RIG method *via* PIM involves three steps: pre-irradiation, grafting copolymerization, and quaternization (Fig. 1) [26,36]. A grafting solution was prepared in a glass reactor for the copolymerization reaction, the solution corresponds to 94 % (*v*/v) of ultrapure water (UPW, 18.2 mΩ), 1 % (v/v) of surfactant 1-octyl-2-pyrrolidone (98 %, Sigma-Aldrich), and 5 % (v/v) of vinylbenzyl chloride monomer (VBC, 90 %, mix de 3 and 4 de isomers, Sigma-Aldrich). The grafting solution was deoxygenated with N_2 for 30 min and, as a sequence, the pre-irradiated HDPE film was added. After adding the film, the reactor was deoxygenated for a further 30 min. When the N_2 flow was stopped, the reactor was immediately closed and heated at 50 °C for 4 h under stirring. The HDPE-grafted film was removed and extensively washed with a toluene and acetone to remove completely any homopolymer and other residues.

The quaternization reaction was carried out by the addition of HDPE-grafted film in an aqueous solution of trimethylamine (TMA, 25 % Vol., Sigma-Aldrich) at RT for 5 h. In the sequence, AEMs were washed with UPW. The AEMs were stocked in chloride form (AEM-Cl^-) to avoid degradation and carbonation. The samples were named in terms of the irradiation parameters (atmosphere and temperature). As an example, the H-RT-air AEM corresponds to pristine HDPE film pre-irradiated under room temperature (RT) and air atmosphere. When referring to the pristine HDPE before grafting and quaternization reactions, the sample the name is followed by the suffix "film".

2.3. Characterization of samples

2.3.1. Degree of grafting (DoG), ion-exchange capacity (IEC), water uptake (WU), thought-plane swelling (TPS), in-plane swelling (IPS), and gel content (GC)

The DoG, which corresponds to the mass of grafts added to the HDPE film, was determined by Eq. (1). The m_g corresponds to the mass of dry grafted-HDPE film, while m_i is the initial mass of the pre-irradiated pristine HDPE film.

$$DoG\ (\%) = \frac{m_g - m_i}{m_i} \times 100 \quad (1)$$

In terms of AEMs, all measurements were carried out in their

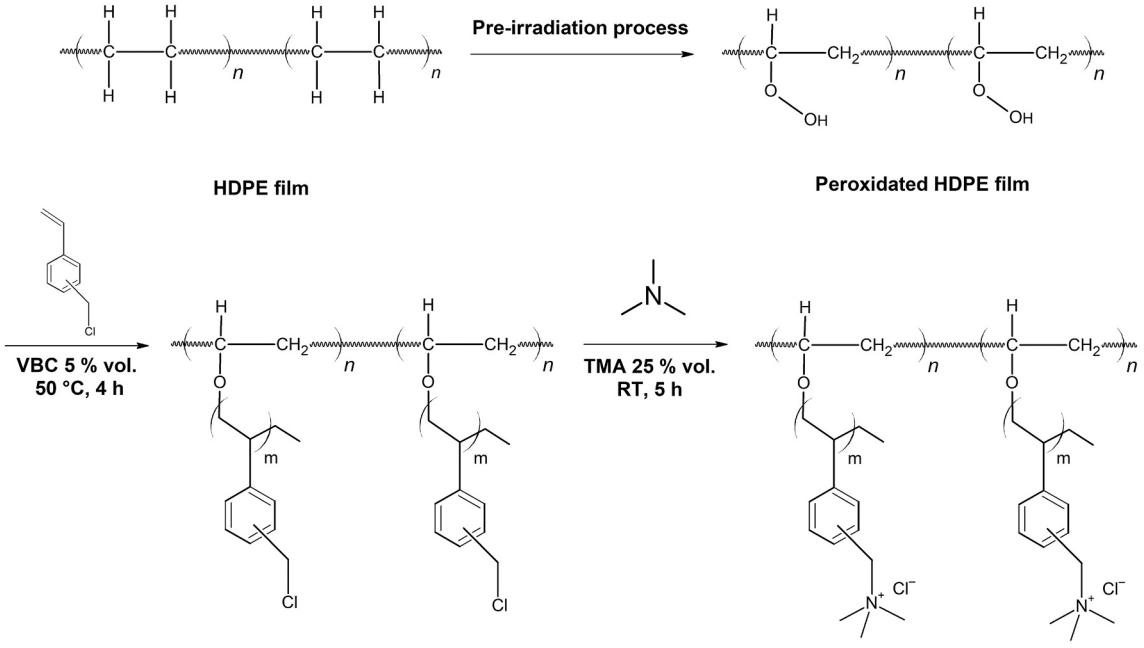

Fig. 1. Steps for preparing AEMs under different pre-irradiation conditions.

chloride form and performed on $n = 3$ samples to ensure the reproducibility of the results. The IEC of AEMs was determined as described elsewhere [40], using a Titrino 848 Plus Metrohm equipment. The AEMs (3 cm × 3 cm) were dried at 50 °C in vacuum oven for 16 h to determine their dry mass (m_{dry}). The samples were soaked in 20 mL of $NaNO_3$ solution 2.3 M for 16 h, and 2 mL of HNO_3 2 M was added. The solution was titrated with a silver nitrate solution ($AgNO_3$, 0.0205 N) up to end point (E_p), which corresponds to first differential plot between the volume data and Ag Titrode potential. The IEC value was estimated by Eq. (2).

$$IEC\ (mmol/g) = \frac{Ep^{*}0.0205}{mdry} \tag{2}$$

The water absorption properties, *i.e.*, WU, TPS and IPS were obtained using Eqs. (3), (4), and (5), respectively. The balance the relative humidity (RH), the AEMs were immersed in UPW for 24 h at room temperature (25 °C). The superficial excess of UPW was removed and the initial mass (m_{hyd}), area (A_{hyd}) and thickness (t_{hyd}) were determined. The AEMs were dried at 50 °C for 16 h, as a sequence, the dry mass (m_{dry}), area (A_{dry}) and thickness (t_{dry}) were immediately determined.

$$WU\ (\%) = \frac{m_{hyd} - m_{dry}}{m_{dry}} \times 100 \tag{3}$$

$$TPS\ (\%) = \frac{t_{hyd} - t_{dry}}{t_{dry}} \times 100 \tag{4}$$

$$IPS\ (\%) = \frac{A_{hyd} - A_{dry}}{A_{dry}} \times 100 \tag{5}$$

The GC consists of an estimate of the amount of crosslinking in polymers [41]. In brief, a Soxhlet extractor separates the insoluble and soluble phases with heated solvent. The insoluble phase corresponds to the amount of crosslinking of the polymer. The GC was determined to HDPE films pre-irradiated to avoid the influence of grafting and amination process. Approximately 100 mg of sample was placed in filtering paper, dried at 50 °C for 24 h. The dry samples were speedily weighed and placed in the Soxhlet extractor. The samples were extracted with xylol (Sigma-Aldrich) at 150 °C for 3 h with at least 6 washings with solvent. Finally, the filtering papers were dried at 50 °C for 24 h and its mass was recorded. Finally, the Eq. (6) was used to obtain the GC data, where W_i is the weight before extraction and W_f is the final weight.

$$GC\ (\%) = \frac{W_f}{W_i} \times 100 \tag{6}$$

2.3.2. Hydroxide conductivity measurements

The anion conductivity (σ) of the AEMs was determined using a technique described as "*true hydroxide conductivity*", where the carbonation, caused by the reaction of free CO_2 and OH^-, is avoided due to the application of a constant current during the experiment [42–44]. The sample with dimensions of 1 cm × 4 cm was soaked in a solution of potassium hydroxide (KOH, Merck, > 85 %) 1 M to ion exchange of Cl^- to OH^- anions. The sample was washed with UPW, the thickness was determined and then placed in a BT-112 cell with 4-probe from Scribner Associates. The BT-122 cell was sandwiched with a fuel cell device and coupled to an 850e fuel cell test station from Scribner Assoc. In the first step, a constant voltage of 0.8 V was applied for 3 h at 40 °C, RH = 100 % under N_2 flow (99.9992 %) of 0.5 L min^{-1} to decarbonation of samples. After complete decarbonation, verified by a decrease in resistance, the cell temperature was varied from 30 to 80 °C, and a scanning DC sweep from −0.1 V to 0.1 V was carried out 6 times, at 10 min intervals, following a conditioning period (2 h) at the set temperature. The conductivity data was obtained using Eq. (7).

$$\sigma = \frac{d}{R\ x\ w\ x\ t} \tag{7}$$

where d = 0.425 cm, *w*, *t*, *R* are the width, thickness and resistance of the hydrated AEM samples, respectively.

2.3.3. Mechanical and thermal properties

The stretch-strain measurements were carried out exclusively in pre-irradiated samples (RT-air, RT-N_2, LT-air, and LT-N_2) to verify the effects of the radiation on the mechanical properties of the HDPE backbone and avoid the grafting effects under HDPE structure. The samples with rectangular dimensions of 1 cm × 5 cm were placed in pneumatic tensile grips in an Instron 5567 instrument with a speed of 2 mm min^{-1}, using a load of 1 kN at RT. To guarantee reproducibility, at least 5 identical specimens were tested for each sample.

Pre-irradiated pristine HDPE films and AEMs were analyzed by thermal techniques, such as differential scanning calorimetry (DSC) and

thermogravimetric analysis (TGA). A TGA/DSC +3 Mettler Toledo was used to perform the DSC measures. Approximately 5 mg of the sample was trapped in an aluminum pan, and the equipment was programmed to work between 25 and 160 °C, rate of 5 °C min^{-1}, under N_2 flow of 20 mL min^{-1} for 3 cycles of heating-cooling-heating. The melting temperature (T_m) and the melting enthalpy (ΔH_m) were obtained by second heating, while the crystallization temperature (T_c) and crystallization enthalpy (ΔH_c) crystallization were obtained by cooling cycle. The ΔH_m data was used to determine the crystallinity (X_C) of the samples using Eq. (8).

$$X_C = (\Delta H_m/\Delta H_\infty)x100 \quad (8)$$

where $\Delta H_\infty = 288.9$ J/g is the melting enthalpy of 100 % crystalline PE [45].

Thermogravimetric analysis (TGA/DTG) was performed using TG/DTA/SDT Q600 model TA. The measures were performed (~10 mg of sample) in a temperature range of 30 to 700 °C with rate of 10 °C min^{-1}, under nitrogen flow of 50 mL min^{-1}.

2.3.4. Raman spectroscopy

Raman spectra of AEMs were collected with an excitation laser wavelength source of 1064 nm, laser power of 600 mW performed with 128 scans in a FT-Raman spectrometer multi-Raman from Bruker Optics.

2.4. Morphological characterizations

The synchrotron small angle x-ray scattering (SAXS) measurements were performed in European Synchrotron Radiation Facility (ESRF), France at DUBBLE BM26 line [46]. The dried AEMs with 5 sheets (~4 mm thick) were stacked in DSC aluminum pans and covered with mica windows to avoid scattering. The tests occurred in a Linkam DSC600 setup at 25 °C and 15 s of exposition of the x-ray beam. The distance between the detector and samples (PILATUS 1 M 169 mm × 179 mm active area) was of 4 m, radiation wavelength (λ) of 0.124 nm and energy of 12.4 keV. The scattering angle range for the SAXS was calibrated with the pattern of AgBe. The bubble software [47] was used to diminish the intensity in the 2D detectors to 1D intensity profiles performing a correct the incident intensity fluctuations and background subtraction, as a function of the scattering vector ($q = 4\pi/\lambda \sin\theta$), taking into account the sample transmission effect.

Surface topographic images of the AEMs in Cl^- form were obtained by atomic force microscopy (AFM) using an Agilent 5500 AFM/SPM microscope. The series of samples were dried in a vacuum oven at 50 °C for 24 h. Each sample was placed on the AFM's sample holder using adhesive tape and gently pressed to level the surface and minimize irregularities. The surface of each sample was scanned in soft tapping mode using a NanoWorld Pointprobe® NCST AFM probe, with a resonance frequency of 160 kHz, and a force constant of 7.4 N/m. The scan rate was set at 0.3 lines per second. Images were captured over an area of 10 × 10 μm with a resolution of 256 × 256 pixels. The topographic parameters, including root mean square roughness (Rrms) and average roughness (Ra) were analyzed using the free software WSxM 5.0 Develop 10.3 [48].

Scanning electron microscopy (SEM) images of the AEMs in Cl^- form were acquired using a JEOL FESEM JSM6701F microscope, operating at a voltage of 1 kV. The samples were dried in a vacuum oven at 50 °C for 24 h, and then gently pressed onto carbon tape to achieve a uniform surface. The carbon tape with the sample was affixed to aluminum specimen mounts and subsequently coated with a thin layer of gold to reduce the charging effect and improve the quality of the images. All measurements in this section were conducted on AEMs in the chloride form to avoid the degradation and carbonation effects associated with alkaline media.

2.5. Preparation of gas diffusion electrode (GDE), membrane electrode assembly (MEA) and fuel cell test

The GDEs with geometric area of 5 cm^2 and Pt loading of 0.50 ± 0.03 mg cm^{-2} were prepared using the spray coating method. The cathode GDE ink was prepared with 80 wt% of commercial Pt/C catalyst from Alfa Aesar (HiSPEC 4000, Pt nominally 40 wt%, supported on carbon) for total solid mass, and 20 wt% of anion-exchange ionomer (AEI) homemade powder of the total solid mass. The AEI (IEC = 2.20 ± 0.01 mmol g^{-1}) employed was a poly(ethene-*co*-tetrafluoroethene) (ETFE) powder grafted with VBC, and quaternized with TMA [49]. The experimental methodology detailed for AEI synthesis is described in section 1.0 at Supplementary Material (SM). The anode catalyst GDE ink was prepared with 53 wt% of commercial PtRu/C from Alfa Aesar (HiSPEC 12,100, Pt nominally 40 wt%, and Ru nominally 20 wt%, supported on carbon) for the total solid mass, 20 wt% of AEI powder, and an extra amount of carbon Vulcan XC-72 correspondent to 27 wt% of the total solid mass. In both cases, the inks were prepared following a procedure described elsewhere [50], where the catalyst powder was ground thoroughly using a pestle for about 5 min, or until visually ensuring a homogenous slurry; there after 1 mL of UPW, and 9 mL of isopropyl alcohol were added. The inks were homogenized in ultrasound for 30 min, sprayed onto carbon paper (Toray TGP-H-60, Teflonated) using an airbrush (Neo Iwata), and then dried in air.

For the AEMFC tests, the AEMs (4 cm × 4 cm) and GDEs were previously maintained in KOH solution (1 M) for 30 min for ionic exchange of Cl^- to OH^-. The MEA was built between two graphite plates with serpentine channels type, intercalating the gasket, anode electrode, membrane, cathode electrode, and gasket. The fuel cell device (5 cm^2 from Scribner Associates) was assembled with a torque of 5.5 N m, and subsequently connected to a 850e Scribner Associates test station. The tests were carried out at 80 °C with a flow of 1 L min^{-1} of H_2 (99.999 %) at the anode and O_2 (99.998 %) at the cathode. The AEMFC humidification temperatures were set between 70 and 72 °C under ambient pressure, and the polarization curves were performed by galvanostatic mode.

2.6. Short-term stability tests

The *ex-situ* short-term stability test was used to evaluate AEM degradation, critical for studying how irradiation conditions affect AEM stability. Isolating membrane effects in AEMFC *in-operando* durability tests is a challenge due to various influencing factors, such as the membrane, catalyst, ionomer, and water management [51]. Thus, evaluating AEMs independently provides clearer insight into their stability. The stability test of the AEMs was performed with similar test parameters to Section 2.3.2 to measure the *"true hydroxide conductivity"* of the samples to mimic the environment of an AEMFC in operation for 100 h. In this case, after de-carbonation step, the cell temperature was fixed at 80 °C and RH of 80 % under N_2 (99.9992 %) flow of 0.5 mL min^{-1}. A constant voltage of 0.4 V was used to generate a current of 100–200 μA and avoid carbonation. The conductivity was monitored every 30 min during the experiment and the rate of normalized conductivity loss (in percentage) was obtained by linear regression of results.

3. Results and discussion

3.1. Characterization of pre-irradiated HDPE films and AEMs

3.1.1. AEMs physicochemical characteristics

HDPE films were pre-irradiated with 100 kGy under different temperatures (RT or LT) and atmosphere (air or N_2) conditions. The pre-irradiated films were submitted to grafting step with VBC and further functionalized by the amination process with TMA to obtain the AEMs. The physicochemical properties of AEMs, such as DoG, IEC, and WU are

shown in Fig. 2. When comparing AEMs exposed to identical irradiation atmosphere but different temperatures, H-RT-air *vs.* H-LT-air or H-RT-N_2 *vs.* H-LT-N_2, it is evident that in both cases (air and N_2), the DoG is higher for LT-samples. On the other hand, the comparison between AEMs irradiated in distinct atmospheres but at same temperature, H-RT-air *vs.* H-RT-N_2 or H-LT-air *vs.* H-LT-N_2, has not shown an obvious trend for atmosphere effect. The DoG of H-RT-N_2 > H-RT-air (155 *vs.* 136 %, respectively) and the DoG of H-LT-air is slightly higher than H-LT-N_2 (190 *vs.* 183 %, respectively). The DoG values are normally associated with the amount of available radicals generated within the polymer upon exposure to ionizing radiation, which subsequently participate in the grafting reaction [35,52]. The amount of radicals as well as their nature depend on the different irradiation parameters, including the absorbed dose, dose rate, temperature, and atmosphere conditions which are related to radiolysis events of C—H and C—C bonds present in the PE polymer [53,54]. To verify the trend between DoG and the amount of available radicals after the pre-irradiation process, fast electron paramagnetic resonance (EPR) measurements were performed on pre-irradiated HDPE films 24 h after irradiation (prior to grafting step). The EPR spectra (see Fig. S1) display a multiplet signal in the magnetic field region between 3400 and 3600 G. The multiple peaks result from the overlapping signals of various radical types, including alkyl, allyl, polyenyl, and oxidized radicals, such as peroxyl and hydroperoxyl, which form during the irradiation process [55,56]. To estimate the number of radicals generated, the peak-to-peak (pph) parameter (representing the intensity of the central peaks of each spectrum) was calculated. The analysis revealed that the estimated population of radicals follows the exact same trend as the DoG: H-RT-air < H-RT-N_2 < H-LT-N_2 < H-LT-air (see Fig. S1). LT samples consistently exhibited higher radical population compared with RT-samples, regardless of the atmosphere. As expected, the DoG parameter strongly correlates with the number of radicals generated during the treatment applied to the HDPE films.

Analyzing the parameters studied, in this work, the irradiation atmosphere seems to have less influence than the temperature on the DoG, especially at low temperature. Our previous researches using low-density polyethylene (LDPE) [36] and ethylene-*co*-tetrafluoroethylene (ETFE) [22] films also highlighted the relevance of irradiation temperature as a crucial factor for controlling the DoG. Interestingly, these previous studies [22,36] have shown lower DoG values for LDPE or ETFE-based membranes prepared under similar irradiation conditions (samples irradiated with 100 kGy at LT and air atmosphere) than the current HDPE-based AEMs, with DoGs = 125, 143, and 190 %, respectively. This feature can be related to the starting film thickness, which was smaller for HDPE films (10 μm of HDPE *vs.* 25 μm of LDPE and ETFE), and/or to the polymer intrinsic properties, such as chains arrangement or hydrophobicity, impacting the grafting front mechanism [57].

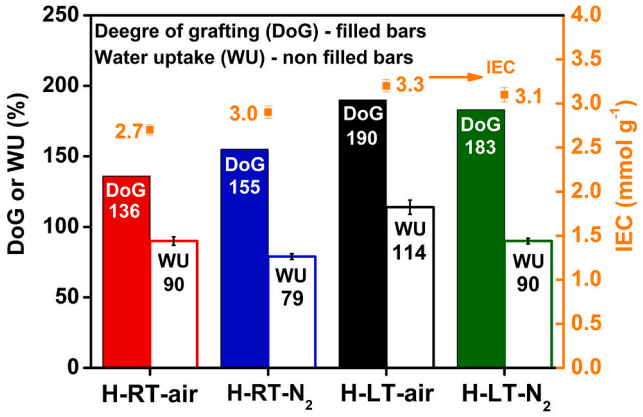

Fig. 2. The degree of grafting (DoG), ion-exchange capacity (IEC), and water uptake (WU) characteristics of HDPE-based AEMs prepared under different conditions of irradiation.

Fig. 2 demonstrates that although the samples exhibit different DoG values, there is minimal variation in the IECs among the four synthesized membranes: H-LT-air (3.30 mmol g^{-1}) > H-LT-N_2 (3.12 mmol g^{-1}) ≈ H-RT-N_2 (3.0 mmol g^{-1}) > H-RT-air (2.72 mmol g^{-1}). In addition, all these IECs are relatively high compared to previous studies using the same starting HDPE material [5,23].

Normally, it is expected that the IEC follows the DoG in samples synthesized by the same method. Previous studies [6,20,24] have shown that the IEC depends on the number of QA groups inserted in the grafted polymer. Varied amounts of poly(VBC) grafted onto the HDPE film (*i.e.*, DoG) will yield different quantities of available sites for the amination reaction with TMA, ultimately leading to a proportional increase in the IEC. However, our results suggest that there is a maximum capacity for QA groups that the polymer can accommodate, also observed by Wang et al. [6]. Additionally, some -CH_2Cl groups of the grafted VBC will react with each other to form crosslinks and will not be available for amination reaction. Therefore, an increase in DoG will not necessarily lead to a markedly higher IEC, as shown by Fig. 2.

Although high DoGs and IECs typically lead to higher WU values [6], the WU for the studied AEMs in the Cl^- form at RT (Fig. 2) did not exhibit a direct correlation with either the IEC or DoG. The measurements were conducted on AEMs in the chloride form to minimize experimental errors associated with carbonation which can occur for AEMs in the OH^- form [58]. The water absorption properties of AEMs in the OH^- form were included for comparative purposes (Fig. S2a) and have shown higher values than those in the Cl^- form at RT as expected. However, these values may be influenced by carbonation during sample preparation and testing, which introduces uncertainties to the measurements. Nonetheless, no clear correlation between WU and IEC or DoG was observed in the OH^- form either. Fig. S2, further demonstrates that the AEMs water absorption properties exhibit a positive correlation with temperature, with increased WU and swelling observed at higher temperatures.

Some studies [24,59,60] concluded that the WU is normally proportional to the IEC, however it is also highly influenced by the degree of crosslinking in the membrane. The degree of crosslinking can be estimated by calculating the Gel Content (GC) of a polymer, in which the fraction of a sample that is insoluble in a particular solvent and a measurable property are associated with the crosslinked portion of the polymer [41]. Since the irradiation step plays a crucial role in polymer crosslinking [22], GC values were quantified for the pre-irradiated HDPE films as shown in Table 1.

In Table 1, all irradiated films display a higher GC value than that of the pristine HDPE film, confirming the formation of crosslinking between polymer chains induced by radiation. Among pre-irradiated samples at the same temperature but in different atmospheres (H-RT-air-film *vs.* H-RT-N_2-film or H-LT-air-film *vs.* H-LT-N_2-film), a higher degree of crosslinking is observed in films irradiated in inert atmosphere. Under N_2 atmosphere, the absence of oxygen molecules prevents the decay of free radicals to peroxide and hydroperoxide species. This

Table 1
Left: Gel content (GC) of the pre-irradiated HDPE films, prior to grafting reaction. Right: Properties of the synthesized AEMs in Cl^- form: ion-exchange capacity (IEC), through-plane swelling (TPS), and in-plane swelling (IPS). The AEM properties were placed next to the pre-irradiated film GC for better visualization of the properties correlations.

HDPE-film	GC (%)	AEM	IEC (mmol g^{-1})	TPS (%)	IPS (%)
Pristine HDPE	0	–	–	–	–
H-RT-air-film	42 ± 1	H-RT-air	2.72 ± 0.03	6 ± 1	30 ± 3
H-LT-air-film	25 ± 2	H-LT-air	3.30 ± 0.08	12 ± 2	39 ± 1
H-RT-N_2-film	48 ± 2	H-RT-N_2	3.00 ± 0.02	4 ± 2	21 ± 2
H-LT-N_2-film	31 ± 1	H-LT-N_2	3.12 ± 0.09	10 ± 1	39 ± 1

facilitates free radical recombination between chains and subsequent crosslinking formation [61]. Similarly, films irradiated in the same atmosphere but at different temperatures (H-RT-air-film *vs.* H-LT-air-film, or H-RT-N_2-film *vs.* H-LT-N_2-film) show increased degree of crosslinking when irradiated at RT compared to LT. Mélot et al. [62] indicated that the decay time of radicals can be mitigated when the irradiation is performed at low temperatures, which occurs due to the restrictive effect on the mobility of polymer chains. This fact explains why the LT-irradiated films have lower GC when compared to RT-irradiated films. At RT, there is a considerable increase in the film's local temperature caused by the high energy of the e-beam, leading to faster crosslinking reaction kinetics [36]. These findings are consistent with those reported for LDPE films in our previous study [36].

Considering that the IECs of the samples are very similar, the different values of WU in Fig. 2 can be associated with variations in the polymer microstructure caused by higher or lower degree of crosslinking. Samples with higher GC exhibit lower WU when irradiated at the same temperature or same atmosphere because of increased hydrophobicity. Hence, whether at RT or LT, samples irradiated in N_2 tend to absorb less water than those irradiated in air, due to the higher degree of crosslinking. Likewise, in N_2 or air atmosphere, samples irradiated at RT tend to absorb less water. Refer to Fig. S3 for a direct comparison between these two properties. The dimensional swelling of the corresponding membranes in the Cl^- form (TPS and IPS, Table 1) are in agreement with what was observed for WU for AEMs irradiated in the same atmosphere at RT or LT: H-LT-air > H-RT-air and H-LT-N_2 > H-RT-N_2. However, dimensional swelling did not show strong dependence on the irradiation atmosphere, as also observed for DoG values. It is noteworthy that all synthesized membranes displayed relatively low dimensional swelling when compared, for example, with a similar AEM-HDPE [23] that presented 38 % ± 7 of TPS. TPS and IPS are important indicatives of water absorption in AEMs and must be controlled to preserve their dimensional stability. For example, an excessive swelling can trigger detachment between electrodes and membrane that ultimately results in poor AEMFC performance and durability [63]. Water-related parameters in general are key properties for AEMs structural stability and ion transportation, which in turn, are also fundamental to understand the ionic conduction mechanisms within the membrane [64,65].

3.2. AEMs ionic conductivity in OH^- form

Fig. 3 illustrates the in-plane OH^- conductivity (σ) of the AEMs varying the temperature from 30 to 80 °C at a fixed RH of 100 %. OH^- conductivity is a critical property of AEMs because it significantly impacts the performance of AEMFCs. The OH^- conductivity profile indicates a thermal dependence, suggesting a thermo-activated conduction mechanism. This behavior can be attributed to the increased free volume for ion transport and enhanced OH^- mobility as the temperature rises [66]. The conductivity values also reveal a close correlation with the IEC trend. The H-LT-air and H-LT-N_2 AEMs exhibit the highest IECs (3.3 and 3.1 mmol g^{-1}, respectively) and the identical OH^- conductivities of 208 mS cm^{-1} at 80 °C. Additionally, the H-RT-N_2 AEM exhibits an intermediate conductivity of 199 mS cm^{-1} at 80 °C with IEC = 3.0 mmol g^{-1}, while the H-RT-air AEM presented the lowest conductivity of 149 mS cm^{-1} at 80 °C for an IEC of 2.7 mmol g^{-1}. While the OH^- conductivities and IEC values of H-LT-air, H-LT-N_2, and H-RT-N_2 are closely aligned, the significant drop in conductivity observed for H-RT-air cannot be solely attributed to its lower IEC. This suggests that factors beyond IEC, such as morphology, can also influence OH^- conductivity. Previous studies have linked enhanced ionic conductivity in AEMs to phase separation between hydrophilic and hydrophobic regions, induced by crosslinking, which facilitates ion conduction [66,67]. However, excessive crosslinking can hinder ionic transport by creating physical barriers that obstruct the AEM structure, ultimately impeding ion movement and reducing conductivity. This highlights the importance of balancing crosslinking to optimize conductivity while maintaining structural integrity.

The activation energy (E_a) for OH^- conductivity (σ) was determined from the ln σ *vs.* 1/T plot, revealing an Arrhenius behavior (see Fig. S4) [68]. The calculated E_a values were as follows: H-RT-N_2 (13 ± 0.7 kJ mol^{-1}) ≈ H-LT-N_2 (12 ± 0.1 kJ mol^{-1}) > H-RT-air (11 ± 0.2 kJ mol^{-1}) > H-LT-air (9 ± 0.5 kJ mol^{-1}), which are consistent with similar AEMs described in the literature [32,90]. The narrow differences in the E_a observed among the AEMs suggest that factors such as hydration levels and nanostructural organisation may contribute to their conduction behavior.

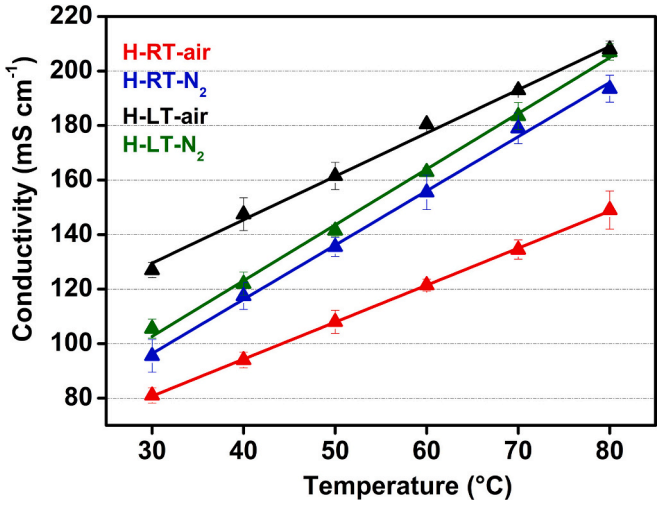

Fig. 3. Temperature-dependence of the in-plane OH^- conductivity of AEMs from 30 to 80 °C at RH = 100 %.

3.3. Mechanical properties

Fig. 4 shows the uniaxial tensile tests conducted on the pre-irradiated HDPE films to examine the impact of irradiation on the polymer's mechanical properties aiming to isolate any influence from grafting or amination steps (see the stress-strain curves at Fig. S5). The elastic modulus (E_m) of all irradiated samples was found to be higher than that

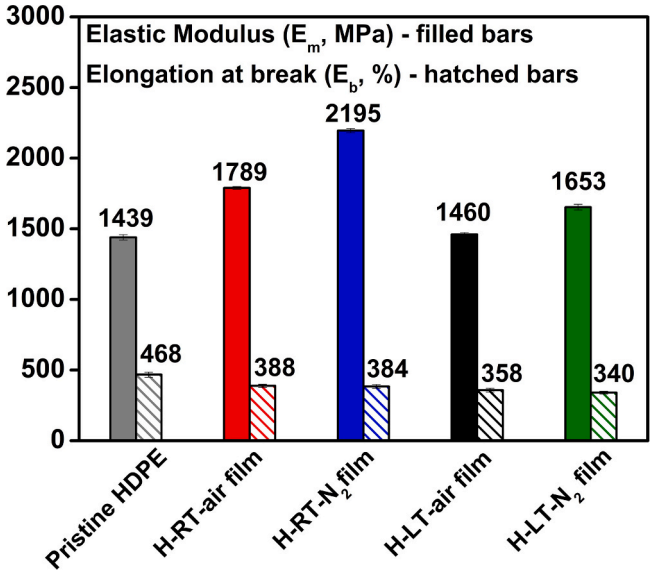

Fig. 4. The mechanical properties, the E_b and E_m results of pristine HDPE and HDPE films irradiated.

of the pristine HDPE film (1439 MPa), indicating a stiffening of the material due to crosslinking induced by radiation. Conversely, the elongation at break (E_b) decreased for all samples compared to the pristine HDPE film (468 %) likely due to a combination of factors including polymer embrittlement from chain scission during irradiation and stiffening of the samples due to radiation-induced crosslinking [26]. Increasing the crosslinking density generally results in a stiffer material with a higher E_m. However, an excessively high crosslinking density can lead to brittle material, thus compromising its elongation properties [22].

Among samples irradiated under identical atmospheres, H-RT-air-film/H-LT-air-film and H-RT-N_2-film/H-LT-N_2-film, it is observed a decreased E_m for films irradiated at LT (1789 > 1460 MPa and 2195 > 1653 MPa, respectively). Likewise, the E_b followed a similar trend by showing smaller values for LT irradiated samples (H-RT-air-film = 388 % *vs* H-LT-air-film = 358 %, and H-RT-N_2-film = 384 % *vs* H-LT-N_2-film = 340 %). For samples irradiated in different atmospheres at the same temperature, irradiation in an inert atmosphere appears to result in a higher E_m and a less evident difference in E_b compared to irradiation in air at both RT and LT. These findings are consistent with the GC data in Table 1, in which the crosslinks are more pronounced in samples irradiated at RT than those irradiated at LT. Likewise, samples irradiated in N_2 exhibit a higher E_m than those irradiated at the same temperature but air atmosphere. The increase in the E_m indicates reinforcement in the polymeric nanostructure network due to crosslinking.

Among all samples, the H-RT-N_2-film exhibits the highest elastic modulus, which is consistent with its GC result shown in Table 1. Despite its high elastic modulus value, this sample demonstrates significant preservation of its elongation capacity, showcasing a good example of improvement in radiation conditions towards obtaining AEMs with enhanced properties.

3.4. Thermal properties

Thermal properties are an important factor that must be considered for AEMs used in fuel cells. The DSC and TGA measures were performed to evaluate the effect of the irradiation condition (RT, LT, air and/or N_2) on thermal properties of irradiated HDPE films and AEMs. Fig. S6 shows the melting characteristics of pristine and irradiated HDPE films. It can be seen from Fig. S6 that the pristine HDPE melting temperature (T_m) of 137 °C and crystallization temperature (T_c) of 118 °C are in good agreement with values found in the literature [69]. When analyzing the thermal properties obtained for pre-irradiated HDPE films, it is possible to observe only a slight change in both the T_m (134–137 °C) and T_c (117–119 °C) values. This reveals that the radiation parameters were not able to affect the thermal properties, preserving these characteristics. On the other hand, the crystallinity plays a crucial role in the thermal properties of semi-crystalline polymers, being associated with the degree of crosslinking. Considering that the crosslinking is significantly affected by radiation conditions, it is pertinent to correlate such effect with crystallinity. The influence of crosslinking on the degree of crystallinity (X_c) of PEs is known [70] (see Table S1), the crosslinking reduces the mobility of polymer chains, consequently diminishing the quantity of crystallizable polymer [69,70]. However, X_c obtained from melting enthalpy (ΔH_m) of DSC runs (Fig. S6) for pre-irradiated samples exhibits a minimal variation in the X_c: H-RT-air-film (48 %) > H-LT-air-film (46 %) > pristine HDPE (43 %) > H-LT-N_2-film (42 %) > H-RT-N_2-film (41 %). The values of X_c indicate that the irradiation protocol applied to samples has no significant effect on the crystallinity. In addition, a crystalline structure preserved should be the crucial factor for keeping the mechanical strengths of the polymer's matrix to some extent.

In terms of thermal characteristics of AEMs (see Table S1 and Fig. S7) no appreciable changes were observed for T_m (127 °C for all) among the samples, but the T_m value diminishes when compared with pristine HDPE (137 °C). Likewise, the same T_c (117 °C for all) value was obtained for all AEMs samples. The thermal profile obtain by TGA/DTG exhibited in Fig. S8 showed that the loss weight for all AEMs is similar with four main events: (1) desorption of water bonded to the TMA group at 30 to 120 °C; (2) break of TMA covalent bonds at 185 to 286 °C [7]; (3) degradation of the poly(VBC) grafts at 374 to 442 °C and [59]; (4) degradation of HDPE backbone at 449 to 519 °C [71].

These findings show that the grafting process can affect the T_m when comparing with pristine HDPE film due to the addition of another polymer (poly(VBC)) with a different nature, however, it cannot change the crystallization process in general terms. In addition, a slight difference in the TGA/DTG profile among the samples is due to the variation in the DoG for each AEM.

3.5. Raman spectroscopy

The functional groups of the molecular structure of AEMs were identified by Raman spectroscopy (Fig. S9) to confirm the synthesis, following a previously report for a similar HDPE-based AEM [23]. Raman bands identified at 1297 and 1448 cm^{-1} are attributed to two vibration modes (-CH_2 twisting and -CH_2 bending, respectively) of the methylene group present in the HDPE structure. The band at 1128 cm^{-1} corresponds to the C—C stretching mode associated to the HDPE backbone [60]. The grafts of the VBC groups in the AEM molecular structure were identified through the Raman bands at 1608 cm^{-1} and 1002 cm^{-1}, which are associated with the benzyl ring stretch, and the *m*-aromatic stretch, respectively [23]. The functionalization of AEMs with TMA was confirmed by the Raman bands found at 976 and 757 cm^{-1}, which are associated with asymmetric and symmetrical stretching of TMA-group [23,61].

3.6. AEMs morphology

The techniques SAXS, AFM, and SEM were employed to investigate the morphological characteristics of the series of AEMs, with SAXS probing the bulk nanostructure and AFM and SEM characterizing the surface. The SAXS profiles shown in Fig. 5 were analyzed from changes in the long-period distance parameter ($D = 2\pi/q_{max}$) of pristine HDPE film to represent the original structure of AEMs. The D was determined by the maximum scattering vector (q), which represents the overall average lamellar thickness between the crystalline and amorphous layers [72,73]. The SAXS profile of pristine HDPE film generates a single peak described as q_1 at 0.257 nm^{-1} that corresponding to long-period of D_1 = 24.4 nm. This result is consistent with previous reports [73].

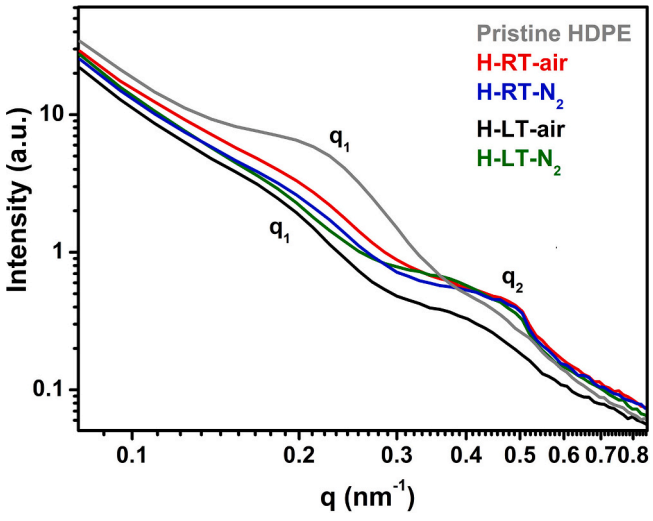

Fig. 5. 1D SAXS intensity profile for pristine-HDPE film and AEMs in the chloride form.

Fig. 5 shows the SAXS profiles for AEMs, where two peaks described as q_1 and q_2 are observed, consequently, the D_1 and D_2 parameters were determined for AEMs. The q_1 in AEMs SAXS profile corresponds to the long-period distance of the base-polymer, *i.e.*, pristine HDPE onto membrane structure. The q_1 parameters of all AEMs were shifted to lower angles when compared with q_1 determined for pristine HDPE. In addition, the q_1 for AEMs exhibits lower intensity which can be attributed to less electron contrast between the amorphous regions and lamellar structures caused by the addition of grafts [74,75]. As a result, the D_1 parameters obtained for AEMs follows: H-LT-air (38 nm) > H-LT-N_2 (37 nm) > H-RT-air (35 nm) > H-RT-N_2 (31 nm). These results reveal an evident change in the nanostructure of AEMs in terms of D_1 when compared with pristine HDPE (D_1 = 24.4 nm). In this case, the grafting process influenced by pre-irradiation conditions, increases the amorphous layer thickness leading to a large distance between the crystalline domains. This find is consistent with the decrease in the X_c for AEMs when compared with pristine HDPE film presented in Table S1, which indicates a lower amount of crystallizable material onto AEMs structure. These factors are consistent with the grafting process. A recent work brought highlights to explain the RIG-polymerization mechanism, where the grafts begin at the interface between the amorphous and crystalline phases of HDPE films [76]. After filling the amorphous phase, the grafts grow to cover the crystalline phase [76].

The appearance of a new peak described as q_2 indicates the formation of the segregation phase of the AEMs structure, which is absent on pristine HDPE and corresponds to the ionic domains of the AEMs described as D_2 [26]. The D_2 appears as a consequence of TMA-groups bonded to VBC groups, which introduce the hydrophilic characteristics for AEMs [26]. Thus, the D_2 of the AEMs exhibits: H-LT-air = 15 nm; H-LT-N_2 = 14.5 nm; H-RT-air = 13 nm; and H-RT-N_2 = 13.5 nm. It is important to mention that the segregation phase creates ionic conduction channels of high mobility within of hydrophilic phase of the membrane improving the hydroxyl conductivity [77,78]. Thus, the differences found in D_2 parameter of each AEMs can be crucial to electrochemical properties given singular characteristics.

The AFM was performed to evaluate how the irradiation protocol can affect the surface features of the AEMs series investigated here. In the topographic images of the samples (Fig. 6), 10 μm × 10 μm scanning area, the dark and bright regions are associated to holes and bulges surface. Fig. 6a shows the AFM image for the pristine HDPE film, which presents an R_{rms} of 142 nm. The R_{rms} analysis from the AFM images for AEMs (Figs. 6b-d), obtained by the different irradiation treatments, shown significant difference in the R_{rms} values, with the following trend: H-RT-N_2 (434 nm) > H-RT-air (320 nm) > H-LT-N_2 (239 nm) > H-LT-air (228 nm). The 3D maps and R_a values can be checked in Fig. S10.

Based on the R_{rms} findings, it is important to note that the roughness of AEMs subjected to irradiation can be related with physicochemical alterations occurring on the polymer's surface. This characteristic is influenced by several factors: i) the effect of the electron beam on the surface can lead to the creation of areas with varying amplitudes as a result of different radiation doses [79], ii) gaseous released during crosslinking and chain scission radiolysis can form bubbles, which subsequently modify the surface roughness [80,81]; iii) for grafted films, the differences in roughness may be linked to the concentration of grafts, resulting in regions with higher and lower amplitudes [82]. Despite this, it is reasonable to mention that the combination of these events is responsible for the final roughness of the surface of the AEMs. However, the R_{rms} values decreased for the LT-samples when compared to the RT-samples. This decrease can be associated with the mitigation of chain scission or crosslinking reactions when the HDPE films were irradiated at low temperature, resulting in fewer gases being generated and consequently decreasing the R_{rms}. Then, this feature suggests that the RT-samples have a more pronounced formation of gases in the bulk of the material during the pre-irradiation likely due to temperature variations that can occur during the process, as previously studied in our group [36].

SEM was used to examine the surface of the AEMs, and the images are presented in Fig. S11. Fig. S11a shows a smooth surface for the pristine HDPE film, whereas the AEM surfaces (Fig. S11b-e) display dense and irregular surface morphologies resulting from the grafting and amination processes. The surface irregularity seems to be more pronounced for H-RT-air and H-RT-N_2 AEMs, while H-LT-N_2 shows a smoother surface. The H-LT-air AEM exhibits alternating smooth and agglomerated regions, primarily for AEMs with high graft amounts. These qualitative observations are consistent with R_{rms} properties obtained through AFM measurements and previously explained. The SEM images reveal no consistent visual pattern on the surfaces of the AEMs that can be directly attributed to the pre-irradiation processes.

3.7. AEMFC tests

Fig. 7 shows the polarization curves obtained from AEMFCs tests at 80 °C with AEMs synthesized under different irradiation conditions. The

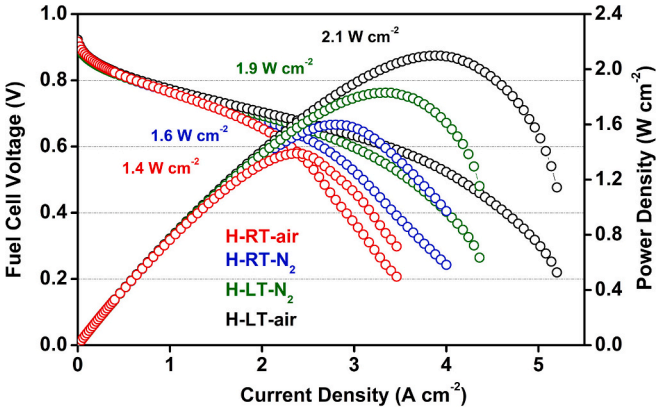

Fig. 7. Polarization curves of AEMFCs performed at 80 °C and atmospheric pressure. O_2 cathode gas flow of 1.0 L min^{-1}, and H_2 anode gas flow of 1.0 L min^{-1}. The anode and cathode gases were operated with an optimal humidification temperature range from 70 to 72 °C. AEMs wet thicknesses: H-RT-air = 28 μm; H-RT-N_2 = 34 μm; H-LT-N_2 = 37 μm; H-LT-air = 38 μm.

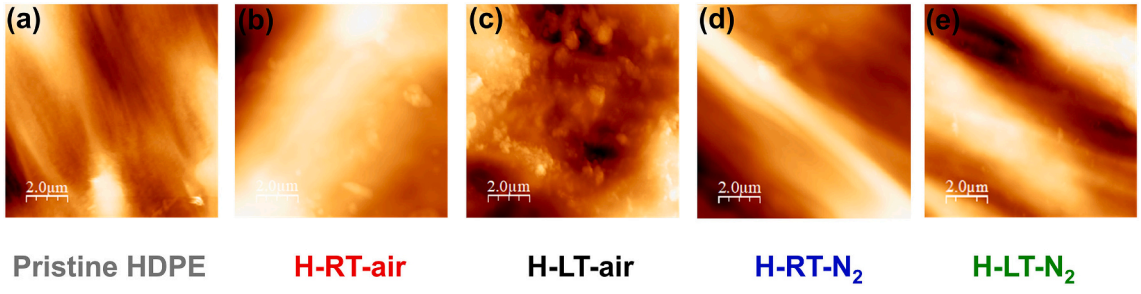

Fig. 6. AFM images with scale of 2 μm for pristine HDPE film (a), and H-RT-air (b), H-LT-air (c), H-RT-N_2 (d), and H-LT-N_2 (e) AEMs.

curves evidenced the same polarization profile with the main differences in ohmic drop as well as mass transport polarization regions, which are water-associated processes. The power peak density obtained by fuel cells performances varied from 1.4 to 2.1 W cm^{-2} and followed the OH^- conductivity trend for all AEMs derivatives. In fact, the membrane's conductivity is considered the main irreversibility of the ohmic drop overpotential, influencing the global performance response of AEMFCs. Taking into account that the irradiation protocol can significantly impact the properties that govern the ionic conduction mechanism on AEMs, *i.e.*, the number of QA's, is reasonable to associate performance with DoG, IEC and/or conductivity. However, the difference in performance for the AEMs is also resulting from a higher overpotential associated with mass limiting transport (current density > 2 A cm^{-2}), which is related to water management.

The irradiation process significantly impacts the morphology and nanostructure of AEMs as evidenced by AFM and SAXS analyzes, and in turn can influence the fuel cell performance. Uncontrolled membrane roughness, for example, can impede homogenous gas distribution, leading to restricted mass transport, hindering catalyst layer adhesion and causing both mechanical stress and electrode delamination [83–85]. The degree of crosslinking, on the other hand, plays a crucial role in the water transportation within the membrane, affecting the overall fuel cell efficiency. Water management is particularly influenced by the intrinsic morphological characteristics of each AEM, which govern the complex movement of water molecules during fuel cell operation. Such feature is a consequence of water transport processes inherent to low-temperature fuel cells, in which electroosmotic drag and vehicular mechanism govern the water management resulting in an imbalance between water generation and consumption at the anode and cathode electrodes [86]. Further research is essential to understand the direct influence of morphology and nanostructure on the performance of fuel cells incorporating RIG-AEMs. Nonetheless, beginning-of-life experiments indicate that pre-irradiation parameters significantly impact power density by enhancing ion conduction properties and optimizing water management. These improvements result from successful radiation grafting and a more favorable morphological profile, making RIG-AEMs highly suitable for fuel cell applications.

3.8. Short-term AEMs stability tests

The AEMs stability was investigated by measuring the loss of conductivity over time at 80 °C and RH of 80 %. The short-term tests were performed at 80 °C to simulate the operating temperature of the AEMFC and under RH of 80 % to accelerate the degradation process during the 100 h of the experiment. The data were normalized to evaluate the percentage loss of conductivity over time (% h^{-1}) (Fig. 8). A voltage was constantly applied to guarantee the absence of carbonate formation in AEMs, as described elsewhere [42–44].

The conductivity loss of the H-RT-air AEM featured the worst stability performance (−0.17 % h^{-1}) while H-RT-N_2 and H-LT-air AEMs presented the best results with degradation rate of ~ −0.06 % h^{-1}. Considering samples irradiated in air, decreasing the temperature during the irradiation process appears to be efficient for stability since degradation rate of the H-LT-air is almost three times lower than that observed for H-RT-air. On the other hand, the opposite has been observed for the pair irradiated in N_2 atmosphere, H-LT-N_2 *vs.* H-RT-N_2, showcasing degradation rates of −0.09 % h^{-1} and -0.06 % h^{-1}, respectively. A similar behavior is observed when analyzing the temperature-fixed, *i.e.*, the comparison H-RT-air *vs.* H-RT-N_2 provides −0.17 % h^{-1} *vs.* -0.06 % h^{-1}, while the comparison between H-LT-air *vs.* H-LT-N_2 exhibits −0.06 % h^{-1} *vs.* -0.09 % h^{-1}. Both H-LT-air and H-RT-N_2 AEMs exhibit identical degradation rates, which makes it difficult to assign the factor among the irradiation parameters that contributes more significantly to chemical stability.

The degradation mechanism of AEMs grafted with poly(VBC)-TMA *via* RIG is described elsewhere [87,88]. In general, specific parts of the

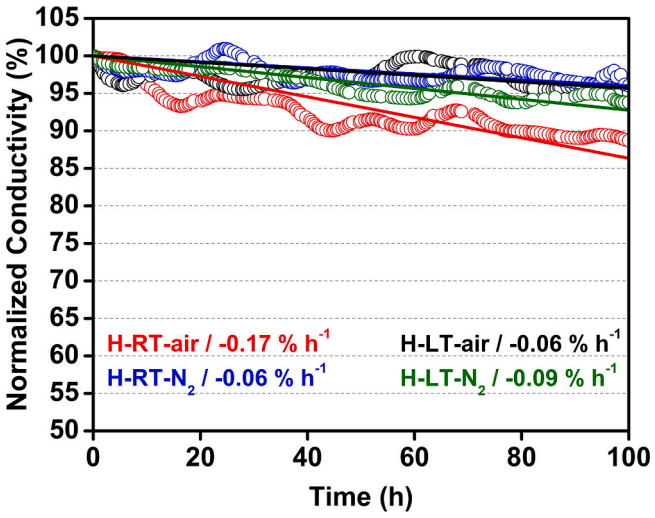

Fig. 8. The normalized loss of hydroxide conductivity at 80 °C in RH of 80 % of the AEMs.

AEM structure are affected by degradative processes, such as pre-fabricated polymer backbone, poly(VBC) grafts (side chains), and the TMA-groups. Likewise, the degradation mechanisms are governed by three reactional routes, which can take place simultaneously: *i*) AEM degradation occurs by the loss of the quaternary ammonium group as a result of nucleophilic substitution bimolecular (S_N2) reaction *via* OH^- attack, leading to the formation of benzylic alcohol and the leave of the tertiary amine group. Although the Hofmann elimination reaction is possible, it does not the preferred route due to H_β is absent in the VBC-TMA group; *ii*) the auto-oxidation/oxidation reactions from peroxide radicals generated in the alkaline media could attack the benzylic carbon in poly(VBC) structure, eliminating VBC-TMA groups of the AEM; *iii*) chain scission reactions by the attack of OH^- ions on the C—C bonds present in AEM backbone, leading to fragmentation of the polymeric structure [87,88].

In this work, the degradation of AEMs during the accelerated durability test was attributed to the irradiation process applied to the samples (pre-irradiation conditions: RT-air, LT-N_2, LT-N_2, or LT-air). Since all samples share the same molecular structure – resulting from identical grafting and amination steps - it is reasonable to attribute the differences in conductivity loss rates to the effects of radiation on the HDPE matrix structure. However, it is worth mentioning that the degradative processes of side chains and quaternary ammonium groups are normally the primary contributors to overall degradation in these types of membranes, and likely follows similar patterns across the AEMs studied. For instance, the degradation of AEMs *via* OH^- attack to the TMA group likely involves the association of three pathways: (i) benzyl alcohol formation by substitution of VBC-$N^+(Me)_3$ by the VBC-OH group; (ii) methyl loss from the VBC-$N^+(Me)_3$, resulting in the formation of tertiary amine VBC-$N(Me)_2$; and (iii) ylide formation through proton abstraction from the benzylic methylene group (benzyl-CH_2-$N^+(Me)_3$), followed by conversion to a tertiary amine (benzyl-CH(Me)-$N(Me)_2$). These potential degradation routes are illustrated in Scheme S1.

Fig. S12 presents mechanical and structural data, including gel content (GC) and elastic modulus, to explore correlations between backbone modifications and stability. The results show no direct correlation between increased crosslinking (estimated by GC) and HDPE-AEM degradation in short-term tests. For instance, H-LT-air and H-RT-N_2 both exhibit the lowest degradation rates, but have opposites GC values, H-LT-air displaying the lowest and H-RT-N_2 the highest. A similar trend is observed for elastic modulus, indicating that crosslinking reinforcement does not play a decisive role in initial stability. Comparisons with previous work on LDPE-based AEMs [36] highlight a

higher degradation tendency for LDPE membranes pre-irradiated at room temperature compared to HDPE membranes. LDPE-LT-air shows a loss rate of $-0.1\ \%\ h^{-1}$ [36] *vs* $-\ 0.06\ \%\ h^{-1}$ for H-LT-air. This difference is likely due to the intrinsic properties of LDPE and HDPE backbones (Table S3). Although pre-irradiation parameters influence degradation, they are only one aspect of the complex, multifactorial degradation mechanism.

4. Conclusion

A series of pre-irradiation protocols were performed to mitigate the damage caused by ionizing radiation used to synthesize HDPE-based anion-exchange membranes. Experimental results show that the AEMs properties can be strongly affected by an inappropriate choice of irradiation protocol, compromising their physicochemical, thermal, mechanical, morphological, and electrochemical characteristics. The findings reveal that the choice of atmosphere during irradiation significantly affects the balance between radical generation and oxidative degradation, with nitrogen environment promoting more crosslinking while air atmosphere can favor oxidative processes. Additionally, lowering the temperature ($\sim -10\ ^{\circ}C$) during the pre-irradiation step effectively preserved radicals in the HDPE film, leading to an improvement in the degree of grafting (DoG) of AEMs. As a result, the ion-exchange capacity (IEC), water uptake (WU), dimensional swelling, and crosslinking characteristics were optimized. The AEMs morphology was also influenced by the changes in the pre-irradiation protocol, which resulted in specific nanomorphology for each membrane, characterized by lamellar distance and surface roughness. The electrochemical properties such as OH^- conductivity (σ) were enhanced for the H-LT-air AEM, reaching $\sigma = 208\ mS\ cm^{-1}$ at 80 °C, which was superior to the standard H-RT-air sample that showed $\sigma = 149\ mS\ cm^{-1}$ at 80 °C. In addition, AEMFC tests achieved a peak power density of $1.4\ W\ cm^{-2}$ at a current density of $2.3\ A\ cm^{-2}$ for H-RT-air AEM, and $2.1\ W\ cm^{-2}$ at a current density of $3.8\ A\ cm^{-2}$ for H-LT-air AEM, representing a 50 % increase in AEMFC performance and placing it within the top-level performance range of current HDPE-based AEMFC technology. Finally, short-term stability tests showed a significant improvement of over 180 % when comparing H-RT-air and H-LT-air AEMs, highlighting the importance of lowering the temperature during the pre-irradiation in air.

CRediT authorship contribution statement

Andrey S. Barbosa: Writing – review & editing, Writing – original draft, Visualization, Methodology, Investigation, Data curation, Conceptualization. **Ana Laura G. Biancolli:** Writing – review & editing, Writing – original draft, Visualization, Investigation, Conceptualization. **Bianca P.S. Santos:** Writing – original draft, Methodology, Investigation, Data curation. **Jean-Jacques Bonvent:** Writing – review & editing, Methodology, Investigation, Data curation. **Daniel Hermida-Merino:** Writing – review & editing, Methodology, Investigation, Data curation. **Elisabete I. Santiago:** Writing – review & editing, Supervision, Resources, Project administration, Funding acquisition, Conceptualization.

Declaration of competing interest

The authors declare that they have no known competing financial interests or personal relationships that could have appeared to influence the work reported in this paper.

Data availability

Data will be made available on request.

Acknowledgements

The authors acknowledge the support from FAPESP (grant no. 2017/11987-4, grant no. 2017/11937-4), Shell, and the strategic importance of the support provided by ANP (Brazil's National Oil, Natural Gas, and Biofuels Agency). A. L. G. B. acknowledges FAPESP for the grant No. 2019/26955-3. The authors also thank CNPq for funding support through IBH2-MCTI No. 405793/2022-7, CNPq SisH2 No. 407967/2022-2, as well as FAPESP for projects No. 2022/07786-9 - (M-ERA.NET) and No. 2024/01763-2. The authors are grateful to Eng. Elizabeth S. Somessari, Dr. Yasko Kodama, and MSc. Djalma B. Dias for their support with the pre-irradiation of HDPE films, tensile tests, and TGA/DTG, all performerd at CETER-IPEN. The authors also thank Dr. Heloísa A. Zen for support with the DSC measurements at CEQMA-IPEN, Dr. Orlando R. Jr. for the support with the EPR measurements at CMR-IPEN, and Dr. Sérgio Damasceno for support with the SEM measurements. Thanks are extended to the UFABC Multiuser Central Facility for access to the Raman, AFM, and SEM equipment. EIS is a fellow of the Brazilian CNPq.

Appendix A. Supplementary data

Supplementary data to this article can be found online at https://doi.org/10.1016/j.reactfunctpolym.2025.106149.

References

[1] H.A. Miller, Green hydrogen from anion exchange membrane water electrolysis, Curr. Opin. Electrochem. 36 (2022) 101122, https://doi.org/10.1016/j.coelec.2022.101122.
[2] J. Li, Q. Liu, L. Tian, W. Ma, F. Wang, Z. Wang, H. Zhu, Novel poly(carbazole-butanedione) anion exchange membranes constructed by obvious microphase separation for fuel cells, Int. J. Hydrog. Energy 47 (2022) 32262–32272, https://doi.org/10.1016/j.ijhydene.2022.07.095.
[3] J. Yang, M.J. Jang, X. Zeng, Y.S. Park, J. Lee, S.M. Choi, Y. Yin, Non-precious electrocatalysts for oxygen evolution reaction in anion exchange membrane water electrolysis: a mini review, Electrochem. Commun. 131 (2021) 107118, https://doi.org/10.1016/j.elecom.2021.107118.
[4] M.M. Hossen, M.S. Hasan, M.R.I. Sardar, J. Bin Haider, K. Tammeveski Mottakin, P. Atanassov, State-of-the-art and developmental trends in platinum group metal-free cathode catalyst for anion exchange membrane fuel cell (AEMFC), Appl. Catal. B Environ. (2022) 121733, https://doi.org/10.1016/j.apcatb.2022.121733.
[5] S. Haj-Bsoul, J.R. Varcoe, D.R. Dekel, Measuring the alkaline stability of anion-exchange membranes, J. Electroanal. Chem. 908 (2022), https://doi.org/10.1016/j.jelechem.2022.116112.
[6] L. Wang, J.J. Brink, Y. Liu, A.M. Herring, J. Ponce-González, D.K. Whelligan, J. R. Varcoe, Non-fluorinated pre-irradiation-grafted (peroxidated) LDPE-based anion-exchange membranes with high performance and stability, Energy Environ. Sci. 10 (2017) 2154–2167, https://doi.org/10.1039/c7ee02053h.
[7] J. Ponce-Gonzalez, D.K. Whelligan, L. Wang, R. Bance-Soualhi, Y. Wang, Y. Peng, H. Peng, D.C. Apperley, H.N. Sarode, T.P. Pandey, A.G. Divekar, S. Seifert, A. M. Herring, L. Zhuang, J.R. Varcoe, J. Ponce-González, D.K. Whelligan, L. Wang, R. Bance-Soualhi, Y. Wang, Y. Peng, H. Peng, D.C. Apperley, H.N. Sarode, T. P. Pandey, A.G. Divekar, S. Seifert, A.M. Herring, L. Zhuang, J.R. Varcoe, High performance aliphatic-heterocyclic benzyl-quaternary ammonium radiation-grafted anion-exchange membranes, Energy Environ. Sci. 9 (2016) 3724–3735, https://doi.org/10.1039/c6ee01958g.
[8] T.Y. Son, D.J. Kim, V. Vijayakumar, K. Kim, D.S. Kim, S.Y. Nam, Anion exchange membrane using poly(ether ether ketone) containing imidazolium for anion exchange membrane fuel cell (AEMFC), J. Ind. Eng. Chem. 89 (2020) 175–182, https://doi.org/10.1016/j.jiec.2020.05.009.
[9] S. Kwon, A.H.N. Rao, T.H. Kim, Anion exchange membranes based on terminally crosslinked methyl morpholinium-functionalized poly(arylene ether sulfone)s, J. Power Sources 375 (2018) 421–432, https://doi.org/10.1016/j.jpowsour.2017.06.047.
[10] B. Xue, F. Wang, J. Zheng, S. Li, S. Zhang, Highly stable polysulfone anion exchange membranes incorporated with bulky alkyl substituted guanidinium cations, Mol. Syst. Des. Eng. 4 (2019) 1039–1047, https://doi.org/10.1039/c9me00064j.
[11] R. Yang, P. Dai, S. Zhang, R.W. Xu, S. Hong, W.F. Lin, Y.X. Wu, In-situ synthesis of cross-linked imidazolium functionalized poly(styrene-b-isobutylene-b-styrene) for anion exchange membranes, Polymer (Guildf) 224 (2021) 123682, https://doi.org/10.1016/j.polymer.2021.123682.
[12] N. Chen, C. Hu, H.H. Wang, J.H. Park, H.M. Kim, Y.M. Lee, Chemically & physically stable crosslinked poly(aryl-co-aryl piperidinium)s for anion exchange membrane fuel cells, J. Membr. Sci. 638 (2021), https://doi.org/10.1016/j.memsci.2021.119685.

[13] D. Cao, F. Nie, M. Liu, X. Sun, B. Wang, F. Wang, N. Li, B. Wang, Z. Ma, L. Pan, Y. Li, Crosslinked anion exchange membranes prepared from highly reactive polyethylene and polypropylene intermediates, J. Membr. Sci. 661 (2022) 120921, https://doi.org/10.1016/j.memsci.2022.120921.
[14] M.M. Hossain, L. Wu, X. Liang, Z. Yang, J. Hou, T. Xu, Anion exchange membrane crosslinked in the easiest way stands out for fuel cells, J. Power Sources 390 (2018) 234–241, https://doi.org/10.1016/j.jpowsour.2018.04.064.
[15] J. Hu, Y. Meng, C. Zhang, S. Fang, Plasma-polymerized alkaline anion-exchange membrane: synthesis and structure characterization, Thin Solid Films 519 (2011) 2155–2162, https://doi.org/10.1016/j.tsf.2010.11.028.
[16] M. Braglia, I.V. Ferrari, L. Pasquini, T. Djenizian, M. Sette, M.L. Di Vona, P. Knauth, Electrochemical synthesis of thin, dense, and conformal anion exchange membranes with quaternary ammonium groups, Electrochim. Acta 265 (2018) 78–88, https://doi.org/10.1016/j.electacta.2018.01.151.
[17] Z. Zhang, T. Xu, Facile synthesis of poly(arylene ether ketone)s with pendent oxyhexyltrimethylammonium groups for robust anion exchange membranes, Polymer (Guildf) 210 (2020) 123035, https://doi.org/10.1016/j.polymer.2020.123035.
[18] B. Shen, H. Pu, Poly (ether sulfone) s with pendent imidazolium for anion exchange membranes via click chemistry, Polymer (Guildf) 207 (2020) 122944, https://doi.org/10.1016/j.polymer.2020.122944.
[19] Z. Feng, G. Gupta, M. Mamlouk, ScienceDirect a review of anion exchange membranes prepared via Friedel-crafts reaction for fuel cell and water electrolysis, Int. J. Hydrog. Energy 48 (2023) 25830–25858, https://doi.org/10.1016/j.ijhydene.2023.03.299.
[20] L. Wang, E. Magliocca, E.L. Cunningham, W.E. Mustain, S.D. Poynton, R. Escudero-Cid, M.M. Nasef, J. Ponce-González, R. Bance-Souahli, R.C.T. Slade, D. K. Whelligan, J.R. Varcoe, An optimised synthesis of high performance radiation-grafted anion-exchange membranes, Green Chem. 19 (2017) 831–843, https://doi.org/10.1039/c6gc02526a.
[21] K.M. Meek, C.M. Reed, B. Pivovar, K.D. Kreuer, J.R. Varcoe, R. Bance-Soualhi, The alkali degradation of LDPE-based radiation-grafted anion-exchange membranes studied using different e: X situ methods, RSC Adv. 10 (2020) 36467–36477, https://doi.org/10.1039/d0ra06484j.
[22] A.L.G. Biancolli, S. Bsoul-Haj, J.C. Douglin, A.S. Barbosa, R.R. de Sousa, O. Rodrigues, A.J.C. Lanfredi, D.R. Dekel, E.I. Santiago, High-performance radiation grafted anion-exchange membranes for fuel cell applications: effects of irradiation conditions on ETFE-based membranes properties, J. Membr. Sci. 641 (2022), https://doi.org/10.1016/j.memsci.2021.119879.
[23] L. Wang, X. Peng, W.E. Mustain, J.R. Varcoe, Radiation-grafted anion-exchange membranes: the switch from low- to high-density polyethylene leads to remarkably enhanced fuel cell performance, Energy Environ. Sci. 12 (2019) 1575–1579, https://doi.org/10.1039/c9ee00331b.
[24] R. Espiritu, M. Mamlouk, K. Scott, Study on the effect of the degree of grafting on the performance of polyethylene-based anion exchange membrane for fuel cell application, Int. J. Hydrog. Energy 41 (2016) 1120–1133, https://doi.org/10.1016/j.ijhydene.2015.10.108.
[25] S.D. Poynton, J.R. Varcoe, Reduction of the monomer quantities required for the preparation of radiation-grafted alkaline anion-exchange membranes, Solid State Ionics 277 (2015) 38–43, https://doi.org/10.1016/j.ssi.2015.04.013.
[26] A.L.G. Biancolli, A.S. Barbosa, Y. Kodama, R.R. de Sousa, A.J.C. Lanfredi, F. C. Fonseca, J.F.Q. Rey, E.I. Santiago, Unveiling the influence of radiation-induced grafting methods on the properties of polyethylene-based anion-exchange membranes for alkaline fuel cells, J. Power Sources 512 (2021), https://doi.org/10.1016/j.jpowsour.2021.230484.
[27] P.P. Sharma, V. Yadav, A. Rajput, V. Kulshrestha, Acid resistant PVDF based copolymer alkaline anion exchange membrane for acid recovery and electrodialytic water desalination, J. Membr. Sci. 563 (2018) 561–570, https://doi.org/10.1016/j.memsci.2018.06.016.
[28] N. Chen, H.H. Wang, S.P. Kim, H.M. Kim, W.H. Lee, C. Hu, J.Y. Bae, E.S. Sim, Y. C. Chung, J.H. Jang, S.J. Yoo, Y. Zhuang, Y.M. Lee, Poly(fluorenyl aryl piperidinium) membranes and ionomers for anion exchange membrane fuel cells, Nat. Commun. 12 (2021), https://doi.org/10.1038/s41467-021-22612-3.
[29] A. Allushi, T.H. Pham, P. Jannasch, Highly conductive hydroxide exchange membranes containing fluorene-units tethered with dual pairs of quaternary piperidinium cations, J. Membr. Sci. 632 (2021) 119376, https://doi.org/10.1016/j.memsci.2021.119376.
[30] A.G. Wright, J. Fan, B. Britton, T. Weissbach, H.F. Lee, E.A. Kitching, T.J. Peckham, S. Holdcroft, Hexamethyl-: P -terphenyl poly(benzimidazolium): a universal hydroxide-conducting polymer for energy conversion devices, Energy Environ. Sci. 9 (2016) 2130–2142, https://doi.org/10.1039/c6ee00656f.
[31] Y. Zhu, L. Ding, X. Liang, M.A. Shehzad, L. Wang, X. Ge, Y. He, L. Wu, J.R. Varcoe, T. Xu, Beneficial use of rotatable-spacer side-chains in alkaline anion exchange membranes for fuel cells, Energy Environ. Sci. 11 (2018) 3472–3479, https://doi.org/10.1039/c8ee02071j.
[32] T.A. Sherazi, J. Yong Sohn, Y. Moo Lee, M.D. Guiver, Polyethylene-based radiation grafted anion-exchange membranes for alkaline fuel cells, J. Membr. Sci. 441 (2013) 148–157, https://doi.org/10.1016/j.memsci.2013.03.053.
[33] X. Peng, D. Kulkarni, Y. Huang, T.J. Omasta, B. Ng, Y. Zheng, L. Wang, J. M. LaManna, D.S. Hussey, J.R. Varcoe, I.V. Zenyuk, W.E. Mustain, Using operando techniques to understand and design high performance and stable alkaline membrane fuel cells, Nat. Commun. 11 (2020), https://doi.org/10.1038/s41467-020-17370-7.
[34] K.L. Lim, C.Y. Wong, W.Y. Wong, K.S. Loh, S. Selambakkannu, N.A.F. Othman, H. Yang, Radiation-grafted anion-exchange membrane for fuel cell and electrolyzer applications: a mini review, Membranes (Basel) 11 (2021) 1–21, https://doi.org/10.3390/membranes11060397.
[35] A. Ashfaq, M.-C. Clochard, X. Coqueret, C. Dispenza, M.S. Driscoll, P. Ulański, M. Al-Sheikhly, Polymerization reactions and modifications of polymers by ionizing radiation, Polymers (Basel) 12 (2020) 2877, https://doi.org/10.3390/polym12122877.
[36] Barbosa, S. Andrey, Biancolli, G. Ana Laura, Alexandre J.C. Lanfredi, Jr Rodrigues, Fonseca Orlando, C. Fábio, Santiago, I. Elisabete, Enhancing the durability and performance of radiation-induced grafted low-density polyethylene-based anion-exchange membranes by controlling irradiation conditions, J. Membr. Sci. 659 (2022), https://doi.org/10.1016/j.memsci.2022.120804.
[37] A. Alsabbagh, R. Abu Saleem, R. Almasri, S. Aljarrah, S. Awad, Effects of gamma irradiation on 3D-printed polylactic acid (PLA) and high-density polyethylene (HDPE), Polym. Bull. 78 (2021) 4931–4945, https://doi.org/10.1007/s00289-020-03349-3.
[38] M. Dole, The Radiation Chemistry of Macromolecules: Free Radicals in Irradiated Polyethylene, New York, 1972.
[39] I. Carpentieri, V. Brunella, P. Bracco, M.C. Paganini, E.M. Brach Del Prever, M. P. Luda, S. Bonomi, L. Costa, Post-irradiation oxidation of different polyethylenes, Polym. Degrad. Stab. 96 (2011) 624–629, https://doi.org/10.1016/j.polymdegradstab. 2010.12.014.
[40] L. Wang, E. Magliocca, E.L. Cunningham, W.E. Mustain, S.D. Poynton, R. Escudero-Cid, M.M. Nasef, J. Ponce-González, R. Bance-Souahli, R.C.T. Slade, D. K. Whelligan, J.R. Varcoe, An optimised synthesis of high performance radiation-grafted anion-exchange membranes, Green Chem. 19 (2017) 831–843, https://doi.org/10.1039/c6gc02526a.
[41] A. D2765-16, Standard Test Methods for Determination of Gel Content and Swell Ratio of Crosslinked Ethylene Plastics, ASTM International, West Conshohocken, 2016, https://doi.org/10.1520/D2765-16.
[42] J. Müller, A. Zhegur, U. Krewer, J.R. Varcoe, D.R. Dekel, Practical ex-situ technique to measure the chemical stability of anion-exchange membranes under conditions simulating the fuel cell environment, ACS Mater. Lett. 2 (2020) 168–173, https://doi.org/10.1021/acsmaterialslett.9b00418.
[43] A. Zhegur-Khais, F. Kubannek, U. Krewer, D.R. Dekel, Measuring the true hydroxide conductivity of anion exchange membranes, J. Membr. Sci. 612 (2020) 118461, https://doi.org/10.1016/j.memsci.2020.118461.
[44] N. Ziv, D.R. Dekel, A practical method for measuring the true hydroxide conductivity of anion exchange membranes, Electrochem. Commun. 88 (2018) 109–113, https://doi.org/10.1016/j.elecom.2018.01.021.
[45] A.J. Peacock, Handbook Polyethylene: Structures, Properties, and Applications, N. Y, 2000, https://doi.org/10.1016/0167-188X(89)90104-3.
[46] G. Portale, D. Cavallo, G.C. Alfonso, D. Hermida-Merino, M. Van Drongelen, L. Balzano, G.W.M. Peters, J.G.P. Goossens, W. Bras, Polymer crystallization studies under processing-relevant conditions at the SAXS/WAXS DUBBLE beamline at the ESRF, J. Appl. Crystallogr. 46 (2013) 1681–1689, https://doi.org/10.1107/S0021889813027076.
[47] V. Dyadkin, P. Pattison, V. Dmitriev, D. Chernyshov, A new multipurpose diffractometer PILATUS@SNBL, J. Synchrotron Radiat. 23 (2016) 825–829, https://doi.org/10.1107/S1600577516002411.
[48] I. Horcas, R. Fernández, J.M. Gómez-Rodríguez, J. Colchero, J. Gómez-Herrero, A. M. Baro, WSXM: a software for scanning probe microscopy and a tool for nanotechnology, Rev. Sci. Instrum. 78 (2007), https://doi.org/10.1063/1.2432410.
[49] A.L.G. Biancolli, D. Herranz, L. Wang, G. Stehlíková, R. Bance-Soualhi, J. Ponce-González, P. Ocón, E.A. Ticianelli, D.K. Whelligan, J.R. Varcoe, E.I. Santiago, ETFE-based anion-exchange membrane ionomer powders for alkaline membrane fuel cells: a first performance comparison of head-group chemistry, J. Mater. Chem. A 6 (2018) 24330–24341, https://doi.org/10.1039/c8ta08309f.
[50] T.J. Omasta, A.M. Park, J.M. Lamanna, Y. Zhang, X. Peng, L. Wang, D.L. Jacobson, J.R. Varcoe, D.S. Hussey, B.S. Pivovar, W.E. Mustain, Beyond catalysis and membranes: visualizing and solving the challenge of electrode water accumulation and flooding in AEMFCs, Energy Environ. Sci. 11 (2018) 551–558, https://doi.org/10.1039/c8ee00122g.
[51] N.U. Hassan, M. Mandal, G. Huang, H.A. Firouzjaie, P.A. Kohl, W.E. Mustain, Achieving high-performance and 2000 h stability in anion exchange membrane fuel cells by manipulating ionomer properties and electrode, Optimization 2001986 (2020) 1–8, https://doi.org/10.1002/aenm.202001986.
[52] K. Saito, K. Fujiwara, T. Sugo, Innovative polymeric adsorbents: radiation-induced graft polymerization, Innov. Polym. Adsorbents Radiat. Induced Graft Polym. (2018) 1–185, https://doi.org/10.1007/978-981-10-8563-5.
[53] M.A. Mulliez, C. Schilling, T.M. Grupp, Influence of irradiation temperature on oxidative and network properties of X-ray cross-linked vitamin E stabilized UHMWPE for hip arthroplasty, Biomed. Res. Int. 2020 (2020), https://doi.org/10.1155/2020/2568428.
[54] M. Slouf, J. Mikesova, J. Fencl, H. Stara, J. Baldrian, Z. Horak, Impact of dose-rate on rheology, structure and wear of irradiated UHMWPE, J. Macromol. Sci. Part B Phys. 48 (2009) 587–603, https://doi.org/10.1080/00222340902837824.
[55] P.S.Y.S.C. Albano, R. Perera, Chraracterization of gamma irradiation pes using ESR, FTIR, and DSC techniques, Polym. Bull. 51 (2003) 135–142, https://doi.org/10.1007/s00289-003-0206-4.
[56] E. Suljovrujic, Post-irradiation effects in polyethylenes irradiated under various atmospheres, Radiat. Phys. Chem. 89 (2013) 43–50, https://doi.org/10.1016/j.radphyschem.2013.04.003.
[57] W.H. Lee, C. Crean, J.R. Varcoe, R. Bance-Soualhi, A Raman spectro-microscopic investigation of ETFE-based radiation-grafted anion-exchange membranes, RSC Adv. 7 (2017) 47726–47737, https://doi.org/10.1039/c7ra09650j.

[58] U. Krewer, C. Weinzierl, N. Ziv, D.R. Dekel, Electrochimica acta impact of carbonation processes in anion exchange membrane fuel cells, Electrochim. Acta 263 (2018) 433–446, https://doi.org/10.1016/j.electacta.2017.12.093.
[59] B.P.S. Santos, A.S. Barbosa, Y. Kodama, T.B. de Queiroz, E.I. Santiago, Tailoring highly stable anion exchange membranes with graft molecular structure ordering using reversible addition-fragmentation chain transfer polymerization for alkaline fuel cells, J. Membr. Sci. 687 (2023) 122071, https://doi.org/10.1016/j.memsci.2023.122071.
[60] J. Chen, M. Asano, T. Yamaki, M. Yoshida, Preparation of sulfonated crosslinked PTFE-graft-poly(alkyl vinyl ether) membranes for polymer electrolyte membrane fuel cells by radiation processing, J. Membr. Sci. 256 (2005) 38–45, https://doi.org/10.1016/j.memsci.2005.02.005.
[61] A. Singh, Irradiation of polyethylene: some aspects of crosslinking and oxidative degradation, Radiat. Phys. Chem. 56 (1999) 375–380, https://doi.org/10.1016/S0969-806X(99)00328-X.
[62] M. Mélot, Y. Ngono-Ravache, E. Balanzat, Very low temperature irradiation of aliphatic polymers: role of radical migration on the creation of stable groups (O-127), Nucl. Instruments Methods Phys. Res. Sect. B Beam Interact. Mater. Atoms. 208 (2003) 345–352, https://doi.org/10.1016/S0168-583X(03)00892-9.
[63] M.M. Hossain, J. Hou, L. Wu, Q. Ge, X. Liang, A.N. Mondal, T. Xu, Anion exchange membranes with clusters of alkyl ammonium group for mitigating water swelling but not ionic conductivity, J. Membr. Sci. 550 (2018) 101–109, https://doi.org/10.1016/j.memsci.2017.12.062.
[64] Q. Duan, S. Ge, C.Y. Wang, Water uptake, ionic conductivity and swelling properties of anion-exchange membrane, J. Power Sources 243 (2013) 773–778, https://doi.org/10.1016/j.jpowsour.2013.06.095.
[65] Y. Zheng, U. Ash, R.P. Pandey, A.G. Ozioko, J. Ponce-González, M. Handl, T. Weissbach, J.R. Varcoe, S. Holdcroft, M.W. Liberatore, R. Hiesgen, D.R. Dekel, Water uptake study of anion exchange membranes, Macromolecules 51 (2018) 3264–3278, https://doi.org/10.1021/acs.macromol.8b00034.
[66] S. Huang, X. He, C. Cheng, F. Zhang, Y. Guo, D. Chen, Facile self-crosslinking to improve mechanical and durability of polynorbornene for alkaline anion exchange membranes, Int. J. Hydrog. Energy 45 (2020) 13068–13079, https://doi.org/10.1016/j.ijhydene.2020.03.013.
[67] J. Huang, Z. Yu, J. Tang, P. Wang, X. Zhang, J. Wang, X. Lei, High-performance anion exchange membranes based on poly(aryl piperidinium): with interpenetrating ion transport channels induced by fluorinated crosslinking and side chains, Fuel 357 (2024) 129686, https://doi.org/10.1016/j.fuel.2023.129686.
[68] R. Epsztein, E. Shaulsky, M. Qin, M. Elimelech, Activation behavior for ion permeation in ion-exchange membranes: role of ion dehydration in selective transport, J. Membr. Sci. 580 (2019) 316–326, https://doi.org/10.1016/j.memsci.2019.02.009.
[69] H.A. Khonakdar, S.H. Jafari, U. Wagenknecht, D. Jehnichen, Effect of electron-irradiation on cross-link density and crystalline structure of low- and high-density polyethylene, Radiat. Phys. Chem. 75 (2006) 78–86, https://doi.org/10.1016/j.radphyschem.2005.05.014.
[70] A. Paajanen, J. Vaari, T. Verho, Crystallization of cross-linked polyethylene by molecular dynamics simulation, Polymer (Guildf) 171 (2019) 80–86, https://doi.org/10.1016/j.polymer.2019.03.040.
[71] M. Fatima Ezzahrae, A. Nacer, E. Latifa, Z. Abdellah, I. Mohamed, J. Mustapha, Thermal and mechanical properties of a high-density polyethylene (HDPE) composite reinforced with wood flour, Mater. Today Proc. 72 (2023) 3602–3608, https://doi.org/10.1016/j.matpr.2022.08.394.
[72] E.L. Heeley, D.J. Hughes, Y. El, P.G. Taylor, A.R. Bassindale, Morphology and crystallization kinetics of polyethylene / long alkyl-chain substituted polyhedral oligomeric Silsesquioxanes (POSS) nanocomposite blends : a SAXS / WAXS study, Eur. Polym. J. 51 (2014) 45–56, https://doi.org/10.1016/j.eurpolymj.2013.11.020.
[73] Y. Hai, C. Huang, M. Ma, Q. Liu, Y. Wang, Y. Liu, F. Tian, J. Lin, Z. Zhu, SAXS investigation of latent track structure in HDPE irradiated with high energy Fe ions, Nucl. Instruments Methods Phys. Res. Sect. B Beam Interact. Mater. Atoms. 356–357 (2015) 129–134, https://doi.org/10.1016/j.nimb.2015.04.075.
[74] N. Cu, Problems Relating to Long Period Determination in Polyethylene Shish-Kebab Structures 3642, 1997, pp. 36–40.
[75] R.K. Bayer, G.H. Michler, Comparative Study of Size and Distribution of Lamellar Thicknesses and Long Periods in Polyethylene With a Shish-Kebab Structure 31, 1996, pp. 4199–4206.
[76] T. Motegi, M. Omichi, Y. Maekawa, N. Seko, Direct observation of radiation-induced graft polymerization on a polyethylene film, Radiat. Phys. Chem. 214 (2024) 111281, https://doi.org/10.1016/j.radphyschem.2023.111281.
[77] D.W. Shin, M.D. Guiver, Y.M. Lee, Hydrocarbon-based polymer electrolyte membranes: importance of morphology on ion transport and membrane stability, Chem. Rev. 117 (2017) 4759–4805, https://doi.org/10.1021/acs.chemrev.6b00586.
[78] Y. He, J. Zhang, X. Liang, M.A. Shehzad, X. Ge, Y. Zhu, M. Hu, Achieving high anion conductivity by densely grafting of ionic strings, J. Membr. Sci. 559 (2018) 35–41, https://doi.org/10.1016/j.memsci.2018.05.002.
[79] O. Güven, A. Alacakir, E. Tan, An atomic force microscopic study of the surfaces of polyethylene and polycarbonate films irradiated with gamma rays, Radiat. Phys. Chem. 50 (1997) 165–170, https://doi.org/10.1016/S0969-806X(97)00002-9.
[80] D. He, M.N. Bassim, Atomic force microscope study of crater formation in ion bombarded polymer, J. Mater. Sci. 33 (1998) 3525–3528, https://doi.org/10.1023/A:1004634724569.
[81] V. Chavan, A. Kulkarni, S.D. Lee, V. Kanade, D. Lee, H.U. Kim, D.Y. Kim, T. Kim, S. Bhoraskar, V.N. Bhoraskar, S.W. Hong, The effects of alpha irradiation on the optical reflectivity of composite polymers, Radiat. Phys. Chem. 191 (2022) 109832, https://doi.org/10.1016/j.radphyschem.2021.109832.
[82] M.I.M. Azzian, S.F. Mohamad, W.N. Wan Salleh, N.H. Ismail, S.Z.N. Ahmad, M. A. Sazali, O. Guven, Surface modification of PVDF membrane by radiation-induced admicellar polymerization of acrylamide in the presence of cationic surfactant, Radiat. Phys. Chem. 214 (2024) 111309, https://doi.org/10.1016/j.radphyschem.2023.111309.
[83] A. Javed, P. Palafox Gonzalez, V. Thangadurai, A critical review of electrolytes for advanced low- and high-temperature polymer electrolyte membrane fuel cells, ACS Appl. Mater. Interfaces 15 (2023) 29674–29699, https://doi.org/10.1021/acsami.3c02635.
[84] N.A.M. Harun, N. Shaari, N.F.H. Nik Zaiman, A review of alternative polymer electrolyte membrane for fuel cell application based on sulfonated poly(ether ether ketone), Int. J. Energy Res. 45 (2021) 19671–19708, https://doi.org/10.1002/er.7048.
[85] F. Barbir, Materials properties and processes, PEM fuel cells, Theory Pract. (2005) 73–113, https://doi.org/10.1016/B978-0-12-078142-3.50005-7.
[86] W.E. Mustain, Understanding how high-performance anion exchange membrane fuel cells were achieved: component, interfacial, and cell-level factors, Curr. Opin. Electrochem. 12 (2018) 233–239, https://doi.org/10.1016/j.coelec.2018.11.010.
[87] R. Espiritu, B.T. Golding, K. Scott, M. Mamlouk, Degradation of radiation grafted hydroxide anion exchange membrane immersed in neutral pH: removal of vinylbenzyl trimethylammonium hydroxide due to oxidation, J. Mater. Chem. A 5 (2017) 1248–1267, https://doi.org/10.1039/c6ta08232g.
[88] R. Espiritu, B.T. Golding, K. Scott, M. Mamlouk, Degradation of radiation grafted anion exchange membranes tethered with different amine functional groups via removal of vinylbenzyl trimethylammonium hydroxide, J. Power Sources 375 (2018) 373–386, https://doi.org/10.1016/j.jpowsour.2017.07.074.